Probing the dynamical phase transition with a superconducting quantum simulator

Kai Xu,[1,*] Zheng-Hang Sun,[1,*] Wuxin Liu,[2,*] Yu-Ran Zhang,[3] Hekang Li,[1,2] Hang Dong,[2] Wenhui Ren,[2] Pengfei Zhang,[2] Franco Nori,[3,4] Dongning Zheng,[1,5,†] Heng Fan,[1,5,‡] and H. Wang[2,§]

[1]*Institute of Physics, Chinese Academy of Sciences, Beijing 100190, China*
[2]*Interdisciplinary Centre for Quantum Information and Zhejiang Province Key Laboratory of Quantum Technology and Device, Department of Physics, Zhejiang University, Hangzhou 310027, China*
[3]*Theoretical Quantum Physics Laboratory, RIKEN Cluster for Pioneering Research, Wako-shi, Saitama 351-0198, Japan*
[4]*Physics Department, University of Michigan, Ann Arbor, MI 48109-1040, USA*
[5]*CAS Centre for Excellence in Topological Quantum Computation, School of Physical Sciences, UCAS, Beijing 100190, China*

Non-equilibrium quantum many-body systems, which are difficult to study via classical computation, have attracted wide interest. Quantum simulation can provide insights into these problems. Here, using a programmable quantum simulator with 16 all-to-all connected superconducting qubits, we investigate the dynamical phase transition in the Lipkin-Meshkov-Glick model with a quenched transverse field. Clear signatures of the dynamical phase transition, merging different concepts of dynamical criticality, are observed by measuring the non-equilibrium order parameter, nonlocal correlations, and the Loschmidt echo. Moreover, near the dynamical critical point, we obtain the optimal spin squeezing of -7.0 ± 0.8 decibels, showing multipartite entanglement useful for measurements with precision five-fold beyond the standard quantum limit. Based on the capability of entangling qubits simultaneously and the accurate single-shot readout of multi-qubit states, this superconducting quantum simulator can be used to study other problems in non-equilibrium quantum many-body systems.

I. INTRODUCTION

Quantum simulation uses a controllable quantum system to mimic complex systems or solve intractable problems[1,2]. Emergent phenomena in out-of-equilibrium quantum many-body systems[3], e.g., thermalization[4] versus localization[5], and time crystals[6], have attracted considerable attentions using quantum simulation. Recently, the dynamical phase transition (DPT) and the non-equilibrium phase transition in transient time scales have been theoretically studied in the transverse-field Ising model with all-to-all interactions[7–9]. These two transitions can be characterized by a non-equilibrium order parameter[7–10], and the Loschmidt echo associated with the Lee-Yang-Fisher zeros in statistical mechanics[11], respectively. Moreover, recent experimental progress has allowed for the controllable simulation of these exotic phenomena with cold atoms[12,13] and trapped ions[14,15]. Yet, experimental explorations for the dynamics of entanglement, as a valuable resource in quantum information processing, remain limited in the presence of a DPT.

In our experiments, applying a sudden change of the transverse field with a controllable strength, we drive the system, initially in its ground state, out of equilibrium. Accurate single-shot readout techniques enable us to synchronously record the dynamics of all qubits and to observe essential signatures of DPTs and spin squeezing from the dynamical criticality in the Lipkin-Meshkov-Glick (LMG) model.

This work presents a systematic quantum simulation of DPTs with two different concepts, providing an evidence of the relation between the non-equilibrium order parameter and the Loschmidt echo. More importantly, we verify entanglement in spin-squeezed states generated from the dynamical criticality, directly observing squeezing of -7.0 ± 0.8 decibels for 16 qubits.

II. RESULTS

Our quantum simulator is a superconducting circuit with 20 fully-controllable transmon qubits capacitively coupled to a resonator bus $\mathcal{R}$ (Fig. 1A). Sixteen qubits (Q_1–Q_{16}), with XY-control lines, are selected to perform experiments (see Materials and Methods). The resonant frequency of $\mathcal{R}$ is fixed at about 5.51 GHz, while the qubit frequencies are individually tuneable via their Z-control lines, enabling us to engineer the qubit-qubit interactions induced by $\mathcal{R}$. We detune all 16 qubits from $\mathcal{R}$ by, e.g., $\Delta/2\pi \simeq -450$ MHz, to switch on the resonator-mediated interactions between two arbitrary qubits[16]. Simultaneously, identical resonant microwave drives, with a magnitude of h^x, are imposed on all qubits to generate the local transverse fields for the control of a DPT (Fig. 1C). The crosstalk effects of microwave pulses have been precisely corrected to ensure the uniformity of the local fields (see Supplementary Materials). The effective Hamiltonian of the quenched system is

$$H_1/\hbar = \sum_{i\neq j}^{N} \lambda_{ij}(\sigma_i^+\sigma_j^- + \sigma_i^-\sigma_j^+) + h^x \sum_{j=1}^{N} \sigma_j^x, \qquad (1)$$

where $N = 16$, $\lambda_{ij} \equiv g_i g_j/\Delta + \lambda_{ij}^c$ is the qubit-qubit coupling strength, g_j represents the coupling strength be-

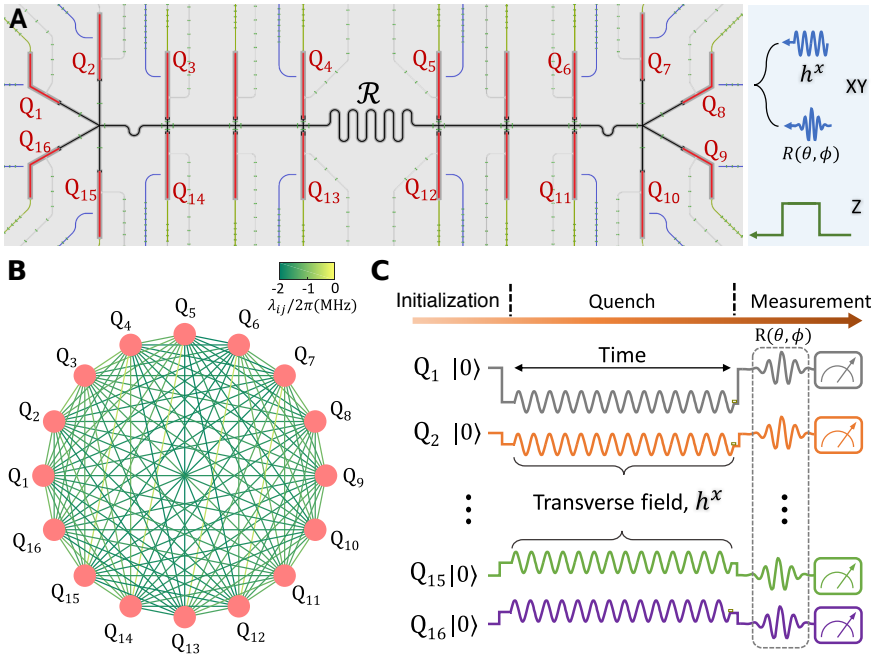

FIG. 1. **Quantum simulator and experimental pulse sequences.** **A**, Optical micrograph of the device with colours added in different regions to distinguish qubits (red), the resonator bus (black), qubit XY-control lines (blue), and Z-control lines (green), respectively. All qubits are capacitively coupled to the resonator bus ($\mathcal{R}$). Each qubit Q_j can be individually controlled by its own Z-control line for the frequency tuning. **B**, Connectivity graph of the 16-qubit system when all qubits are equally detuned from the resonator bus by $\Delta/2\pi \simeq -450$ MHz, with the coloured straight lines representing the magnitude of the qubit-qubit couplings. **C**, The experimental pulse sequences for simulating the DPT. The sequences are divided into three steps. First, the qubits are initialised at the $|00...0\rangle$ state at their corresponding idle frequencies. Then, rectangular pulses are applied to quickly bias each qubit to the same detune from the common resonator bus, to turn on the qubit-qubit interactions. Almost simultaneously, the system is quenched by driving the qubits with resonant microwave pulses for a time t. Finally, the qubits are biased back to their idle frequencies before the 16-qubit joint readout is executed, yielding the probabilities $\{P_{00\ldots0}, P_{00\ldots1}, ..., P_{11\ldots1}\}$, from which $\langle\sigma_j^z\rangle$ can be calculated. When necessary, single-qubit rotation pulses $R_j(\theta_j,\phi_j) = \exp[-i\hbar\theta_j(\cos\phi_j\sigma_j^x + \sin\phi_j\sigma_j^y)/2]$ (in black dotted box) are applied in advance to bring the axis defined by $(\theta_j, \phi_j + \pi/2)$ in the Bloch sphere of Q_j to the σ^z direction before the readout.

tween $\mathcal{R}$ and Q_j, $g_i g_j/\Delta$ is the resonator-induced virtual coupling strength between Q_i and Q_j, which is much larger than the crosstalk coupling λ_{ij}^c (Parameters are shown in Supplementary Materials). Since the values of λ_{ij} are nearly the same for most pairs of qubits and do not decay over a distance $|i-j|$ (Fig. 1B), the quenched system can be reasonably approximated by the LMG model, whose Hamiltonian is $H_{\rm LMG} = (J/N)(\mathcal{S}^z)^2 + \mu\mathcal{S}^x$, with $\mathcal{S}^{x,z} \equiv \sum_j \sigma_j^{x,z}/2$ (see Materials and Methods). Recent studies[7–10,14] have shown that $H_{\rm LMG}$ has a dynamical critical point $\mu/J = 1/2$, separating the dynamical paramagnetic phase (DPP) and the dynamical ferromagnetic phase (DFP) with and without a global $\mathbb{Z}_2$ symmetry, respectively.

First, we show that our programmable superconducting qubits can simulate and verify the DPT by measuring the magnetisation and the spin correlation. The system is initialised at the eigenstate $|00\ldots0\rangle$ of H_1 with $h^x = 0$, where $|0\rangle$ denotes the ground state of a qubit. Then, we quench the system by suddenly adding a transverse field and monitor its dynamics from the time $t = 0$ to 600 ns. With the precise full control and the high-fidelity single-shot readout of each qubit, we are able to omnidirectionally track the evolutions of the average magnetisation

$$\langle\sigma^\alpha(t)\rangle \equiv \frac{1}{N}\sum_{j=1}^{N}\langle\sigma_j^\alpha(t)\rangle,$$

along the x,y,z-axes for different strengths of the quenched transverse fields, with $\alpha \in \{x, y, z\}$. By depicting the trajectory of the Bloch vector $\langle\vec{\sigma}\rangle = [\langle\sigma^x\rangle, \langle\sigma^y\rangle, \langle\sigma^z\rangle]$, the dynamics of our quantum simulator with two distinct transverse fields is visualised in Fig. 2A. For a small transverse field, e.g., $h^x/2\pi \simeq 2$ MHz, $\langle\sigma^z(t)\rangle$ exhibits a slow relaxation (Fig. 2B). However, given a strong transverse field, e.g., $h^x/2\pi \simeq$

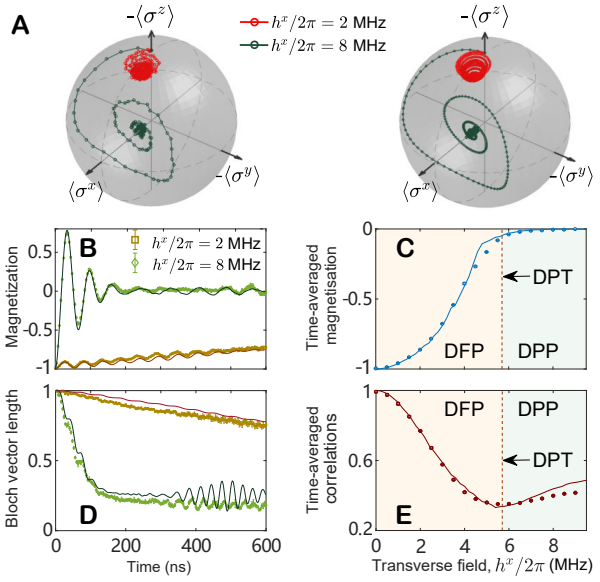

FIG. 2. **Magnetisation and spin correlation. A,** Experimental and numerical data of the time evolution of the average spin magnetisation shown in the Bloch sphere for different strengths of the transverse fields. **B,** The time evolution of the magnetisation $\langle\sigma^z\rangle(t)$. **C,** The nonequilibrium order parameter, $\overline{\langle\sigma^z\rangle}$, as a function of $h^x/2\pi$. **D,** The dynamics of the Bloch vector length $|\langle\vec{\sigma}\rangle|$. **E,** The averaged spin correlation $\overline{C_{zz}}$ versus $h^x/2\pi$. The regions with light red and light blue in **C** and **E** show the dynamical ferromagnetic phase and dynamical paramagnetic phase, respectively, separated by a theoretically predicted critical point $h_c^x/2\pi \simeq 5.7$ MHz. The solid curves in **B–E** are the numerical results using Eq. (1) without considering decoherence.

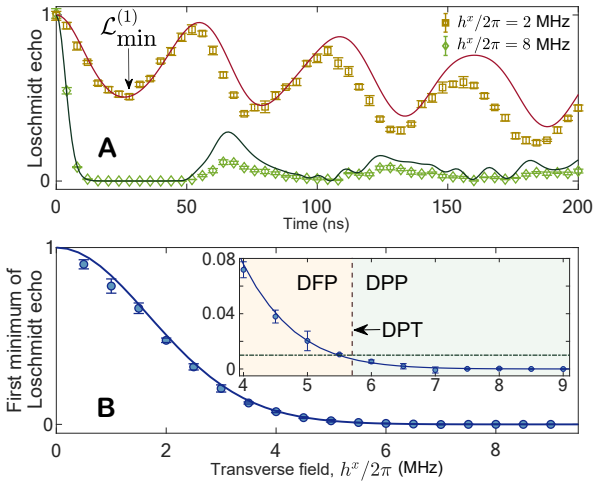

FIG. 3. **Loschmidt echo. A,** Time evolution of the Loschmidt echo $\mathcal{L}(t)$ for different transverse field strengths. **B,** The earliest minimum point of $\mathcal{L}(t)$ during its dynamics, $\mathcal{L}^{(1)}_{\min}$, as a function of h^x. The behaviour of $\mathcal{L}(t)$ for longer time indicates the existence of anomalous dynamical phases[12] (see Methods). Additionally, we note that the Loschmidt echo cannot be strictly equal to 0, because of finite-size effects. We demonstrate that $\mathcal{L}^{(1)}_{\min}$ reaches $\sim 10^{-2}$ at the transition point and becomes smaller in the paramagnetic phase for the LMG model with $N = 16$ (see Methods). The solid curves in **A** and **B** are the numerical results using Eq. (1) without considering decoherence.

8 MHz, $\langle\sigma^z(t)\rangle$ exhibits a large oscillation at an early time and approaches zero in the long-time limit (Fig. 2B). In Fig. 2C, we show the behaviour of the time-averaged magnetisation, $\overline{\langle\sigma^z\rangle} \equiv (1/t_f)\int_0^{t_f} dt\langle\sigma^z(t)\rangle$, that is defined as the non-equilibrium order parameter. It demonstrates that $\overline{\langle\sigma^z\rangle} \neq 0$ and $\overline{\langle\sigma^z\rangle} = 0$ in the DFP and the DPP, respectively. The experimental data of $\overline{\langle\sigma^z\rangle}$ for qubits with different detunings Δ are presented in Supplementary Materials. In addition, the Bloch vector length $|\langle\vec{\sigma}\rangle|$ also depends on the strength of the transverse field h^x. For large h^x, $|\langle\vec{\sigma}\rangle|$ decays rapidly to a small value, indicating strong quantum fluctuations in the DPP[11] (Fig. 2D). Figure 2E shows the averaged spin correlation function, $\overline{C_{zz}} \equiv (1/t_f)\int_0^{t_f} dt \sum_{ij}\langle\sigma_i^z(t)\sigma_j^z(t)\rangle/N^2$, versus h^x with a final time $t_f = 600$ ns, where the DPT is characterised by the local minimum of two-spin correlations[16]. We can observe the critical behaviours of $\overline{\langle\sigma^z\rangle}$ and $\overline{C_{zz}}$ as the signatures of the DPT, when the transverse field strength is set near the theoretical prediction $h_c^x/2\pi = N|\lambda|/8\pi \simeq 5.7$ MHz with $\lambda \equiv \overline{\lambda_{ij}}$ (see Materials and Methods).

Another perspective on dynamical criticality is based on the Loschmidt echo, defined as $\mathcal{L}(t) = |\langle 00\ldots0|e^{-iH_1 t/\hbar}|00\ldots0\rangle|^2$, where the time t, satisfying $\mathcal{L}(t) = 0$, is a Lee-Yang-Fisher zero. The zero will cause the nonanalytical behaviour of the rate function, $r(t) = -N^{-1}\log[\mathcal{L}(t)]$, regarded as the complex-plane generalisation of the free energy density[11]. Recent numerical studies[7,9] have revealed that the existence of Lee-Yang-Fisher zeros closely relates to the DPT between the DFP and the DPP in long-range interacting systems. In Fig. 3A, we show distinct behaviours of the Loschmidt echo in different dynamical phases. Here, we consider the first minimum of the Loschmidt echo $\mathcal{L}^{(1)}_{\min}$ (Fig. 3A), which is sufficient for judging whether the zeros exist or not. It approaches zero in the DPP, and remains relatively large in the DFP[9]. In Fig. 3B, we plot $\mathcal{L}^{(1)}_{\min}$ versus h^x to show the relationship between the DPT and the Loschmidt echo. Similar as the numerical results of the LMG model with finite-size effects (see Methods), we experimentally observe that $\mathcal{L}^{(1)}_{\min} \leq 0.01$ in the DPP, and it becomes relatively large $\mathcal{L}^{(1)}_{\min} > 0.01$ in the DFP. Our work is the first experiment to combine the non-

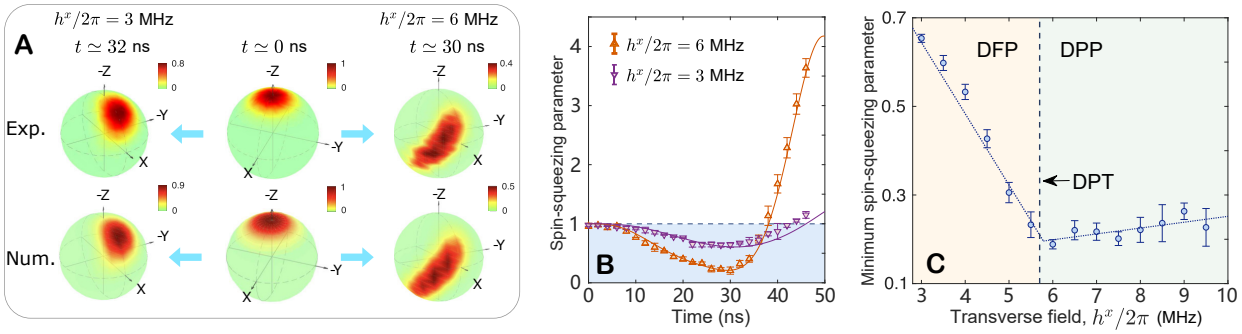

FIG. 4. **Quasidistribution Q-function and spin-squeezing parameter. A,** Experimental and numerical data of $Q(\theta,\phi)$ in the spherical coordinates, when the minimum values of the spin-squeezing parameters are achieved during the time evolutions with the strengths of the transverse fields $h^x/2\pi \simeq 3$ MHz and 6 MHz, respectively. **B,** Time evolution of the spin-squeezing parameters with $h^x/2\pi \simeq 3$ MHz and 6 MHz, respectively. **C,** The minimum spin-squeezing parameter $\xi^2_{\rm min}$ as a function of h^x. The solid lines in **B** are the numerical results using Eq. (1) without considering decoherence. The blue shaded area in **B** is only accessible for entangled states. The dotted line in **C** is the piecewise linear fit, whose minimum point is close to the theoretically predicted critical point $h^x_c/2\pi \simeq 5.7$ MHz (dashed line).

equilibrium order parameter and the Loschmidt echo for verifying a DPT.

In addition to demonstrating a DPT, the LMG model is also useful for generating the spin-squeezed state with twist-and-turn dynamics[17,18]. Near the equilibrium critical point, spin squeezing can be achieved, originating from quantum fluctuations, according to the Heisenberg uncertainty principle[19]. Similarly, we show that the spin-squeezed state can also be generated from the dynamical criticality. During the dynamics of the quenched Hamiltonian (1), we can visualise the spin-squeezed state by measuring the quasidistribution Q-function[20] $Q(\theta,\phi) \propto \langle\theta,\phi|\rho(t)|\theta,\phi\rangle$, where $|\theta,\phi\rangle \equiv \bigotimes_{j=1}^{N}(\cos\frac{\theta}{2}|0\rangle_j + \sin\frac{\theta}{2}e^{i\phi}|1\rangle_j)$ is the spin coherent state. The measurement is realised by applying a single-qubit rotation to bring the axis defined by (θ,ϕ) in the Bloch sphere to the z-axis for each qubit before the joint readout. The experimental and numerical data of $Q(\theta,\phi)$ are compared in Fig. 4A, which clearly show spin squeezing with a large strength of the external field, due to stronger quantum fluctuations in the DPP (see also Fig. 2C).

We also measured the time-evolved spin-squeezing parameter[17] (see Supplementary Materials)

$$\xi^2 = 4\min_{\vec{n}_\perp}[\mathrm{Var}(\mathcal{S}^{\vec{n}_\perp})]/N, \tag{2}$$

where $\vec{n}_\perp$ denotes an axis perpendicular to the mean spin direction, and $\mathrm{Var}(\mathcal{S}^{\vec{n}_\perp}) = \langle(\mathcal{S}^{\vec{n}_\perp})^2\rangle - \langle\mathcal{S}^{\vec{n}_\perp}\rangle^2$. In Fig. 4B, we show that $\xi^2 < 1$ (a sufficient condition for particle entanglement[21,22]) occurs in the time interval $t \lesssim 46$ ns when $h^x/2\pi \simeq 3$ MHz, and for $t \lesssim 38$ ns when $h^x/2\pi \simeq 6$ MHz. The minimum spin squeezing parameter over time, $\xi^2_{\rm min}$, as a function of h^x is shown in Fig. 4C, where the minimum value $\xi^2_{\rm min} \simeq 0.2$ (−7.0 dB) is attained very close to the critical point of the DPT. Compared with the theoretical limit, about $N^{-2/3}$, of the squeezing parameter for an N-body one-axis twisting Hamiltonian[21], our 16-qubit system achieves a spin squeezing parameter satisfying $\xi^2_{\rm min} \simeq N^{-\alpha}$, with $\alpha \simeq 0.58$. It indicates the high-efficiency generation of the spin-squeezed state from dynamical criticality, and reveals the potential application of the DPT in quantum metrology.

III. DISCUSSION

We have presented clear signatures and entanglement behaviors of the DPT in the LMG model with a superconducting quantum simulator featuring all-to-all connectivity, including the non-equilibrium order parameter, the Loschmidt echo, and spin squeezing. Based on its high degree of controllability, precise measurement, and long decoherence time, our platform with all-to-all connectivity is powerful for generating multipartite entanglement[20,23] and investigating non-trivial properties of out-of-equilibrium quantum many-body systems, such as many-body localization[24,25], quantum chaos in Floquet systems[26], and quantum annealing[27].

IV. MATERIALS AND METHODS

A. Device information and system Hamiltonian

The device used here consists of 20 frequency-tuneable superconducting qubits capacitively coupled to a central resonator bus. It is the same circuit presented

in Ref.[20], where more details about the device, the qubit manipulation, and the readout can be found. In Table I (see Supplementary Materials), we present the characteristics for the quantum simulator involving 16 out of the 20 qubits, with XY-control lines, which have been relabelled in the experiments.

The unused four qubits in this device, without XY-control lines, are detuned far off resonance from the other 16 qubits to avoid interacting with them during the experiments. Thus, they will not be included in the following descriptions. The system Hamiltonian, without applying external transverse fields, can be written as

$$H_{s1}/\hbar = \omega_{\mathcal{R}} a^{\dagger}a + \sum_{j=1}^{16}\left[\omega_j(t)|1_j\rangle\langle 1_j| + g_j(\sigma_j^{+}a + \sigma_j^{-}a^{\dagger})\right] + \sum_{i<j}^{16}\lambda_{ij}^{c}(\sigma_i^{+}\sigma_j^{-} + \sigma_j^{-}\sigma_i^{+}),$$

where $\omega_{\mathcal{R}}$ and ω_j represent the fixed resonant frequency and the tuneable frequency of Q_j, respectively, while g_j is the coupling strength between the Q_j and resonator bus. The magnitude of the crosstalk coupling between Q_i and Q_j beyond the resonator-induced virtual coupling is denoted as λ_{ij}^{c}. When equally detuning all the 16 qubits from the resonator bus by about $\Delta/2\pi \simeq -450$ MHz, and simultaneously applying resonant microwaves to each qubit, the system Hamiltonian can be transformed to

$$H_{s2}/\hbar = \sum_{i<j}^{16}(\lambda_{ij}^{c} + g_i g_j/\Delta)(\sigma_i^{+}\sigma_j^{-} + \sigma_j^{-}\sigma_i^{+}) + \sum_{j=1}^{16} h_j^{x}(\sigma_j^{-}e^{i\phi_j} + \sigma_j^{+}e^{-i\phi_j})$$

with $g_i g_j/\Delta$ being the magnitude of the resonator-mediated coupling between Q_i and Q_j. It acts as a dominant part of the qubit-qubit interaction terms, because the crosstalk coupling λ_{ij}^{c} is much smaller. In Fig. 1b, we plot the connectivity graph of the total coupling strength λ_{ij} for all the combinations of pairs of qubits. The individually-controllable amplitude and the phase of the microwave drive on each Q_j are represented by h_j^{x} and ϕ_j, respectively. In our experiments, we set the uniform amplitude and phase for all qubits, leading to the Hamiltonian in Eq. (1) in the main text. To ensure this uniformity, the calibration process for the microwave drives is described in the Supplementary Materials.

B. Relation between the quantum simulator and the LMG model

The experimental technologies ensure that the device can be described via the Hamiltonian in Eq. (1) (H_1) in the main text. With uniform couplings $\lambda \equiv \lambda_{ij}$, the first term of Eq. (1) can be written as

$$\lambda\sum_{i\neq j}^{16}(\sigma_i^{+}\sigma_j^{-} + \text{H.c.}) = (J/N)[\mathcal{S}^2 - (\mathcal{S}^z)^2],$$

where $J \equiv N\lambda$. The second term can be directly rewritten as $h^x\sum_{i=1}^{16}\sigma_i^x = g\mathcal{S}^x$, with $g = 2h^x$. According to $[\mathcal{S}^2, \mathcal{S}^\alpha] = 0$ ($\alpha \in \{x, y, z\}$), and the fact that the initial state $|00\ldots0\rangle$ is an eigenstate of $\mathcal{S}^2$, we have

$$\exp[-i(H_1/\hbar)t]|00\ldots0\rangle \propto \exp(-iH_{\text{LMG}}t)|00\ldots0\rangle,$$

indicating that the dynamical properties of the device H_1 can be approximately expressed as the one of the LMG model

$$H_{\text{LMG}} = -(J/N)(\mathcal{S}^z)^2 + \mu\mathcal{S}^x.$$

The location of the DPT critical point of the LMG model is $\mu_c = |J|/2$, leading to $h_c^x = N\lambda/4$. Note that we only roughly estimate the location of the dynamical critical point of the LMG model. The numerical simulations in the main text are based on the Hamiltonian of the quantum simulator described by Eq. (1) in the main text.

ACKNOWLEDGMENTS

We thank Chao Song, Qiujiang Guo, Zhen Wang, and Xu Zhang for technical support. Devices were made at the Nanofabrication Facilities at the Institute of Physics in Beijing and National Centre for Nanoscience and Technology in Beijing. The experiment was performed on the quantum computing platform at Zhejiang University. This work was supported by the National Basic Research Program of China (Grants No. 2016YFA0302104, No. 2016YFA0300600 and No. 2017YFA0304300), the National Natural Science Foundations of China (Grants No. 11934018, No. 11725419, No. 11434008, and No. 11904393), the Strategic Priority Research Program of Chinese Academy of Sciences (Grant No. XDB28000000), the China Postdoctoral Science Foundation (Grant No. 2018M640055), the AFOSR (Grant No. FA9550-14-1-0040), the ARO (Grant No. W911NF-18-1-0358), the JST Q-LEAP program, the JST CREST (Grant No. JPMJCR1676), the JSPS-RFBR (Grant No. 17-52-50023, the JSPS-FWO (Grant No. VS.059.18N), the JSPS Postdoctoral Fellowship (Grant No. P19326), the RIKEN-AIST Challenge Research Fund, FQXi, and the NTT PHI Lab.

* Those authors contributed equally to this work.
† dzheng@iphy.ac.cn
‡ hfan@iphy.ac.cn
§ hhwang@zju.edu.cn

[1] R. P. Feynman, Simulating physics with computers. *Int. J. of Theor. Phys.* **21**, 467488 (1982).
[2] I. Georgescu, S. Ashhab, F. Nori, Quantum simulation. *Rev. Mod. Phys.* **86**, 153 (2014).
[3] J. Eisert, M. Friesdorf, C. Gogolin, Quantum many-body systems out of equilibrium. *Nat. Phys.* **11**, 124130 (2015).
[4] M. Rigol, V. Dunjko, M. Olshanii, Thermalization and its mechanism for generic isolated quantum systems. *Nature* **452**, 854-858 (2008).
[5] D. A. Abanin, E. Altman, I. Bloch, M. Serbyn, *Colloquium*: Many-body localization, thermalization, and entanglement. *Rev. Mod. Phys.* **91**, 021001 (2019).
[6] N. Y. Yao, A. C. Potter, I.-D. Potirniche, A. Vishwanath, Discrete time crystals: Rigidity, criticality, and realizations. *Phys. Rev. Lett.* **118**, 030401 (2016).
[7] B. Žunkovič, M. Heyl, M. Knap, A. Silva, Dynamical Quantum phase transitions in spin chains with long-range interactions: merging different concepts of nonequilibrium criticality. *Phys. Rev. Lett.* **120**, 130601 (2018).
[8] A. Lerose, J. Marino, B. Žunkovič, B. Gambassi, A. Silva, Chaotic dynamical ferromagnetic phase induced by nonequilibrium quantum fluctuations. *Phys. Rev. Lett.* **120**, 130603 (2018).
[9] B. Gambassi, A. Silva, Chaotic dynamical ferromagnetic phase induced by nonequilibrium quantum fluctuations. *Phys. Rev. Lett.* **120**, 130603 (2018).
[10] B. Sciolla, G. Biroli, Dynamical transitions and quantum quenches in mean-field models. *J. Stat. Mech. Theor. Exper.*, P11003 (2011).
[11] M. Heyl, A. Polkovnikov, S. Kehrein, Dynamical quantum phase transitions in the transverse-field Ising model. *Phys. Rev. Lett.* **110**, 135704 (2013).
[12] N. Fläschner, D. Vogel , M. Tarnowski, B. S. Rem, D.-S. Lühmann, M. Heyl, J. C. Budich, L. Mathey, K. Sengstock, C. Weitenberg, Observation of dynamical vortices after quenches in a system with topology. *Nat. Phys.* **14**, 265268 (2018).
[13] H. Bernien, S. Schwartz, A. Keesling, H. Levine, A. Omran, H. Pichler, S. Choi, A. S. Zibrov, M. Endres, M. Greiner, V. Vuletić, M. D. Lukin, Probing many-body dynamics on a 51-atom quantum simulator. *Nature* **551**, 579584 (2017).
[14] J. Zhang, G. Pagano, P. W. Hess, A. Kyprianidis, P. Becker, H. Kaplan, A. V. Gorshkov, Z.-X. Gong, C. Monroe, Observation of a many-body dynamical phase transition with a 53-qubit quantum simulator. *Nature* **551**, 601604 (2017).
[15] P. Jurcevic, H. Shen, P. Hauke, C. Maier, T. Brydges, C. Hempel, B. P. Lanyon, M. Heyl, R. Blatt, C. F. Roos, Direct observation of dynamical quantum phase transitions in an interacting many-body system. *Phys. Rev. Lett.* **119**, 080501 (2017).
[16] D. I. Tsomokos, S. Ashhab, F. Nori, Fully-connected network of superconducting qubits in a cavity. *New J. Phys.* **10**, 113020 (2008).
[17] M. Kitagawa, M. Ueda, Squeezed spin states. *Phys. Rev. A* **47**, 5138 (1993).
[18] J. Ma, X. Wang, C. P. Sun, F. Nori, Quantum spin squeezing. *Phys. Rep.* **509**, 89165 (2011).
[19] I. Frérot, T. Roscilde, Quantum critical metrology. *Phys. Rev. Lett.* **121**, 020402 (2018).
[20] C. Song, K. Xu, H. Li, Y.-R. Zhang, X. Zhang, W. Liu, Q. Guo, Z. Wang, W. Ren, J. Hao, H. Feng, H. Fan, D. Zheng, D.-W. Wang, H. Wang, S.-Y. Zhu, Generation of multicomponent atomic Schrdinger cat states of up to 20 qubits. *Science* **365**, 574577 (2019).
[21] L. Pezzè, A. Smerzi, M. K. Oberthaler, R. Schmied, P. Treutlein, Quantum metrology with nonclassical states of atomic ensembles. *Rev. Mod. Phys.* **90**, 035005 (2018).
[22] A. sørensen, L.-M. Duan, J. I. Cirac, P. Zoller, Many-particle entanglement with Bose-Einstein condensates. *Nature* **409**, 6366 (2001).
[23] C. Song, K. Xu, W. Liu, C.-p. Yang, S.-B. Zheng, H. Deng, Q. Xie, K. Huang, Q. Guo, L. Zhang, P. Zhang, D. Xu, D. Zheng, X. Zhu, H. Wang, Y.-A. Chen, C.-Y. Lu, S. Han, J.-W. Pan, 10-qubit entanglement and parallel logic operations with a superconducting circuit. *Phys. Rev. Lett.* **120**, 050507 (2018).
[24] K. Xu, J.-J. Chen, Y. Zeng, Y.-R. Zhang, C. Song, W. Liu, Q. Guo, P. Zhang, D. Xu, H. Deng, K. Huang, H. Wang, X. Zhu, D. Zheng, H. Fan, Emulating many-body localization with a superconducting quantum processor. *Phys. Rev. Lett.* **119**, 180511 (2017).
[25] Q. Guo, C. Cheng, Z.-H. Sun, Z. Song, H. Li, Z. Wang, W. Ren, H. Dong, D. Zheng, Y.-R. Zhang, R. Mondaini, H. Fan, H. Wang, Observation of energy resolved many-body localization. arXiv: 1912.02818 (2019).
[26] C. Neill, P. Roushan, M. Fang, Y. Chen, M. Kolodrubetz, Z. Chen, A. Megrant, R. Barends, B. Campbell, B. Chiaro, A. Dunsworth, E. Jeffrey, J. Kelly, J. Mutus, P. J. J. O'Malley, C. Quintana, D. Sank, A. Vainsencher, J. Wenner, T. C. White, A. Polkovnikov, J. M. Martinis, Ergodic dynamics and thermalization in an isolated quantum system, *Nat. Phys.* **12**, 1037-1041 (2016).
[27] W. Lechner, P. Hauke, P. A. Zoller, Quantum annealing architecture with all-to-all connectivity from local interactions. *Sci. Adv.* **1**, e1500838 (2015).
[28] B. Žunkovič, A. Silva, M. Fabrizio, Dynamical phase transitions and Loshmidt echo in the infinite-range XY model, Phil. *Trans. R. Soc. A* **374**: 20150160 (2018).

Supplementary material for 'Probing dynamical phase transitions with a superconducting quantum simulator'

Device parameters. In Table I, we present the characteristics for the quantum simulator involving 16 out of the 20 qubits, with XY-control lines, which have been relabelled in the experiments.

Correction of XY crosstalk. The characterisation of the Z-crosstalk effect and its correction have been described in Ref. 3, which are also the same as in this experiment. In addition, the XY-drive crosstalks between qubits must be corrected, as all qubits are driven by identical microwave drives to quench the system. Different from the Z-crosstalk effects, the characterisation of the XY-crosstalk effects includes the phase calibration of the microwave drives. Fig. 5 shows the calibration process taking the measurement of the XY crosstalk effect of Q_2 to Q_1 as an example.

In Fig. 5a, to characterise the crosstalk amplitude, Q_1 is biased to the interacting frequency $\omega_I/2\pi$, while Q_2's frequency is tuned to a nearby one, e.g., $\omega_I/2\pi - 0.08$ GHz (other qubits are decoupled from Q_1 and Q_2 by tuning their resonant frequencies far away). We apply a strong flattop-envelop microwave pulse with frequency ω_I to Q_2's XY-control line, generating a crosstalk excitation on Q_1. We then monitor the evolution of Q_1's excitations for different resonant frequencies $(\omega_I - \delta_1)$ of Q_1 (δ_1 is a small deviation). By fitting the Rabi oscillation of the measured excited probabilities of Q_1, we can obtain the crosstalk amplitude of Q_2 to Q_1.

In Fig. 5b, we characterise the crosstalk phase of Q_2 to Q_1, with the same frequency arrangement as that in Fig. 5a. However, to cancel the crosstalk effect of Q_2 to Q_1, a microwave pulse on Q_1's XY-control line, with amplitude equal to the crosstalk amplitude of Q_2 to Q_1, should also be added. In this process, we monitor the evolution of Q_1's excitations for different phases of the microwave pulses on Q_2's XY-control line, while fixing the microwave phase of Q_1 to zero. The excitations of Q_1 are almost completely inhibited during the whole evolution process at a specific phase, as can be seen from Fig. 5b, showing that the phase difference of the microwave drives on the XY-control lines of Q_1 and Q_2 is π.

Calibrations of other pairs of qubits are performed with a similar method. After quantifying these crosstalk effects, we correct these issues in experiments by considering the case which only involves two qubits Q_1 and Q_2. We bias these two qubits to $\omega_I/2\pi$ and simultaneously apply resonant microwave pulses on their XY-control lines with amplitudes $Ae^{i\phi_A}$ and $Be^{i\phi_B}$ for Q_1 and Q_2, respectively (other qubits are decoupled from Q_1 and Q_2 by tuning their resonant frequencies far away). Here ϕ_A and ϕ_B represent the microwave phases of Q_1 and Q_2, respectively. If no correction is made, the microwave amplitude and phase of each qubit can be represented as

$$\begin{bmatrix} Ae^{i\phi_A} + a_{12}Be^{i(\phi_{12}+\phi_B)} \\ a_{21}Be^{i(\phi_{21}+\phi_B)} + Be^{i\phi_B} \end{bmatrix} = \tilde{M}_{xy}^{Q_1,Q_2} \begin{bmatrix} Ae^{i\phi_A} \\ Be^{i\phi_B} \end{bmatrix},$$

where

$$\tilde{M}_{xy}^{Q_1,Q_2} = \begin{bmatrix} 1 & a_{12}e^{i\phi_{12}} \\ a_{21}e^{i\phi_{21}} & 1 \end{bmatrix}$$

is the XY-crosstalk matrix measured with the technique described above. On the contrary, if we set the microwave amplitudes and phases of the qubits to $A'e^{i\phi'_A}$ and $B'e^{i\phi'_B}$ in advance, the microwaves we apply to the XY-control lines should be corrected as

$$(\tilde{M}_{xy}^{Q_1,Q_2})^{-1} \begin{bmatrix} A'e^{i\phi'_A} \\ B'e^{i\phi'_B} \end{bmatrix}.$$

We have performed experiments to verify the validity of this XY-crosstalk correction, where we bias Q_1 and Q_2 to ω_I to open the interaction and simultaneously apply identical microwaves to these two qubits. The results are displayed in Fig. 6, demonstrating the validity of this correction. The same treatment can be easily extended to the multi-qubit case.

Note that in the experiments we apply two kinds of microwave drives on the qubits. One establishes the transverse field with the same driving frequency ω_I for all qubits, and the other is the rotation pulse applied at each qubit's idle frequency. The XY-crosstalk correction is only applied when we impose microwave drives on all the qubits, to generate the identical transverse fields. As for the rotation pulses, the XY-crosstalk effects are negligible due to the large detuning between the idle points of qubits.

Calibration of the transverse field. The term of the local transverse field $h_j^x\sigma_j^x$ for each Q_j in Eq. (1) in the main text is enabled by the resonant microwave drives with calibrated magnitude and phase. To ensure the uniformity of the driving magnitude, we perform Rabi oscillation measurements on each stand-alone qubit Q_j at the interacting frequency ω_I. The qubit exposed to the resonant microwave drive will experience an oscillation of its excited-state probability, where the oscillation frequency h_j^x/π can be adjusted by the driving amplitude. For the phase calibration of the transverse field, when applying microwave drives with a flattop envelop to each Q_j, we actually obtain the form $h_j^x(e^{-i\phi_j}\sigma_j^+ + e^{i\phi_j}\sigma_j^-)$, where ϕ_j is the microwave phase sensed by each Q_j and may be different from each other, because of the length disparities between each Q_j's XY-control wires. The experiments require the uniformity of ϕ_j, which can be

	$\omega_j/2\pi$ (GHz)	$T_{1,j}$ (μs)	$T^*_{2,j}$ (μs)	$g_j/2\pi$ (MHz)	$\omega^r_j/2\pi$ (GHz)	$\omega^m_j/2\pi$ (GHz)	$F_{0,j}$	$F_{1,j}$
Q_1	4.835	33	1.7	27.6	6.768	4.815	0.979	0.928
Q_2	5.290	21	1.8	27.4	6.741	5.292	0.970	0.913
Q_3	5.330	37	1.8	29.1	6.707	5.350	0.978	0.920
Q_4	4.460	36	2.0	26.5	6.649	4.420	0.953	0.907
Q_5	4.791	32	2.8	29.2	6.611	4.792	0.980	0.893
Q_6	4.870	30	2.1	30.1	6.558	4.850	0.989	0.938
Q_7	4.569	25	2.2	24.1	6.551	4.450	0.980	0.933
Q_8	5.250	31	2.0	27.7	6.513	5.245	0.978	0.925
Q_9	4.680	23	2.4	27.3	6.524	4.765	0.967	0.926
Q_{10}	4.960	23	1.5	26.9	6.550	4.735	0.972	0.946
Q_{11}	4.899	32	1.6	29.1	6.568	4.880	0.985	0.924
Q_{12}	5.176	22	2.0	26.3	6.640	4.310	0.993	0.941
Q_{13}	5.220	34	2.0	26.5	6.659	5.205	0.987	0.942
Q_{14}	4.490	43	0.9	29.0	6.712	4.583	0.976	0.923
Q_{15}	4.415	>30	1.9	24.6	6.788	4.375	0.967	0.944
Q_{16}	4.766	37	1.5	27.5	6.758	4.906	0.970	0.945

TABLE I. **Quantum simulator characteristics.** Here, ω_j is the idle frequency of Q_j, where single-qubit rotation pulses are applied. $T_{1,j}$ and $T^*_{2,j}$ are the energy relaxation time and Ramsey dephasing time (Gaussian decay) of Q_j, respectively, which are measured at the interacting frequency ω_I (= $\omega_{\mathcal{R}}+\Delta$); g_j denotes the coupling strength between Q_j and the resonator bus $\mathcal{R}$; ω^r_j is the resonant frequency of Q_j's readout resonator; ω^m_j is the resonant frequency of Q_j at the beginning of the measurement process, when its readout resonator is pumped with microwave pulse. Finally, $F_{0,j}$ ($F_{1,j}$) is the probability of detecting Q_j in the $|0\rangle$ ($|1\rangle$) state, when it is prepared in the $|0\rangle$ ($|1\rangle$) state.

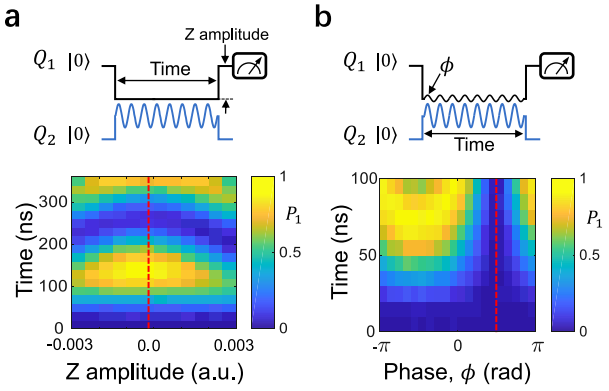

FIG. 5. **Quantification of XY-crosstalk effects. a**, Experimental sequence and results for measuring the XY-crosstalk amplitude. After tuning Q_1 to the interacting point ω_I, we apply a strong microwave drive ($h^x_2/2\pi \simeq$15 MHz) on Q_2's microwave drive line with resonant frequency ω_I. The strong drive will generate a crosstalk Rabi oscillation on Q_1. We measure the Rabi oscillations for different values of δ_1, among which the one with the slowest Rabi oscillation characterises the crosstalk amplitude, as shown by the red dotted line. **b**, Experimental sequence and results for the measurement of the XY-crosstalk phase. In our experiments, we add a microwave drive on Q_1's XY-control line with an adjustable phase ϕ. The selection of ϕ can induce an enhancement or neutralisation effect (red dotted vertical line) on Q_1's Rabi oscillation, which can help us identify the XY-crosstalk phase.

achieved by the following calibration process. Here, we consider two qubits (Q_1 and Q_j), equally detuned from the resonator bus by $\Delta/2\pi \simeq -450$ MHz and driven by resonant microwaves through their own XY-control lines with the driving phases of these two qubits set to 0 and ϕ_j, respectively. The two-qubit Hamiltonian can be written as

$$H_{1j}/\hbar = \lambda_{1j}(\sigma^-_1\sigma^+_j + \sigma^-_j\sigma^+_1) + h^x(\sigma^x_1 + e^{-i\phi_j}\sigma^+_j + e^{i\phi_j}\sigma^-_j),$$

where λ_{1j} is the coupling strength between Q_1 and Q_j, and h^x represents the driving magnitude on the two qubits. In experiments, we start with the ground state and monitor the evolution of the two-qubit system under the above Hamiltonian for different values of ϕ_j. We select Q_1 as the reference and adjust the ϕ_j of other qubits to make them pairwise aligned with that of Q_1. Note that when performing the phase check of Q_1 and Q_j at the interacting point ω_I, the frequencies of other qubits are arranged in the vicinity (about 50 to 100 MHz away from ω_I) to minimise the Z-crosstalk effect. The calibration sequence and experimental results for different ϕ_j are displayed in Fig. 7.

Phase calibration of the rotation pulse. As can be seen from Fig. 1c, after the evolution under the quenched Hamiltonian, we apply the rotation pulse on each qubit before the joint readout to measure the physical quantities, including the average spin magnetisations $\langle\sigma^x(t)\rangle$

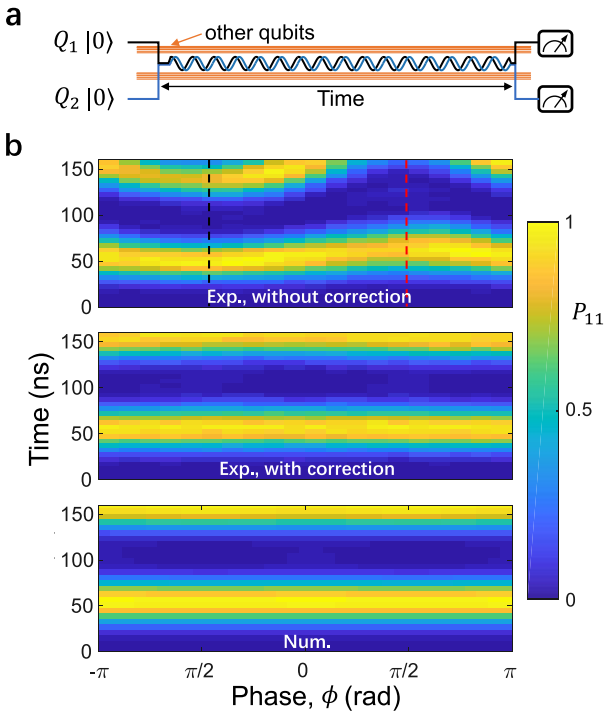

FIG. 6. **Experimental test of the XY-crosstalk correction. a**, The experimental sequence. We tune two qubits on resonance at ω_I, while other qubits are arranged in the vicinity, and apply resonant microwave drives ($h^x/2\pi \simeq 5$ MHz for each qubit) on these two qubits's XY-control lines with a controllable phase difference of ϕ. **b**, The measured probabilities P_{11} of the $|11\rangle$-state, versus t and ϕ, in cases with and without applying the XY-crosstalk correction, compared with the numerical results. When no XY-crosstalk correction is made, the measured oscillation periods of P_{11} for different ϕ values show an obvious inconsistency, indicating an enhancement (black dotted vertical line) or neutralisation (red dotted vertical line) effects induced by the XY crosstalk. After applying the XY-crosstalk correction, the experimental results are in good agreement with the numerical results.

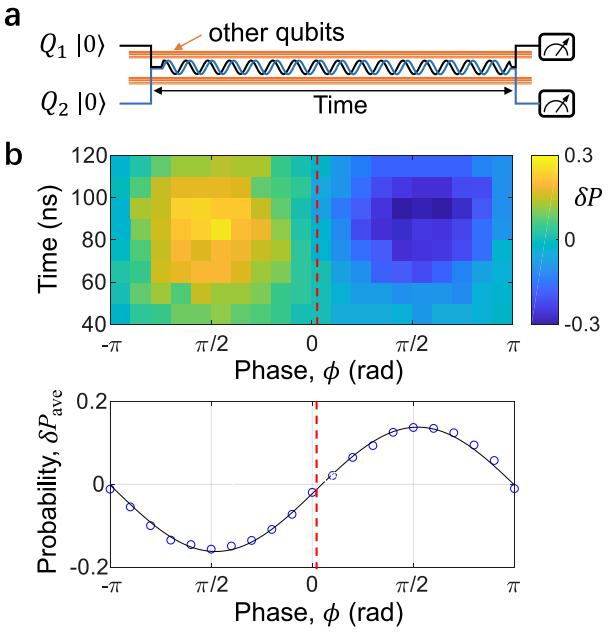

FIG. 7. **Phase alignment of the transverse field. a**, Experimental sequence. Two qubits (Q_1 and Q_2) are detuned from the resonator bus $\mathcal{R}$ by the same amount $\Delta/2\pi \simeq -450$ MHz, while other qubits are arranged in the vicinity of this point to minimise Z-crosstalk effects. We then apply resonant microwave drives on these two qubits with the same magnitude ($h^x/2\pi \simeq 2$ MHz) but a phase difference of ϕ and monitor the dynamics from 40 ns to 120 ns by recording the probabilities of Q_1 and Q_2, denoted as $P_1^{Q_1}$ and $P_1^{Q_2}$. **b**, 2D graph of $\delta P \equiv P_1^{Q_2} - P_1^{Q_1}$ as a function of t and ϕ (top) and the time-averaged δP (bottom). We fit this curve with a sine function to extract the phase offset (red dotted vertical line), which will be added to the microwave drive of Q_2 to ensure the phase alignment between these two qubits.

and $\langle\sigma^y(t)\rangle$. The rotation operation on each qubit is realised by a Gaussian-envelope microwave pulse with a full width at half maxima of 20 ns, which has been characterised by randomised benchmarking with a fidelity above 0.99 for both $X_{\pi/2}$ and $Y_{\pi/2}$ rotation gates.

To mainly compensate for the dynamic phase caused by frequency tuning through the sequence, the phase of each rotation pulse needs to be corrected. The calibration process is presented in Fig. 8a, taking Q_1 as an example. The calibrated qubit is biased to the interacting frequency ω_I with a rectangular pulse, while the frequencies of other qubits are arranged in the vicinity to minimise the Z-crosstalk effect. Almost simultaneously, Q_1 is driven by a flattop-envelope microwave pulse with frequency ω_I. Then, we bias Q_1 back to its idle frequency and apply a $\pi/2$-rotation pulse before the readout. We record the probabilities of Q_1's excited state during this dynamics for different phases ϕ of the rotation pulse. The results are displayed in Fig. 8b, where the phase offset used for the correction is highlighted by the red dotted vertical line.

Measurement of the spin-squeezing parameter. The calculation of the spin-squeezing parameter ξ^2 consists of the following steps. The first step is to calculate the mean-spin direction $\vec{n}_0 = (\sin\theta\cos\phi, \sin\theta\sin\phi, \cos\theta)$, where

$$\theta = \arccos\left(\frac{\mathcal{S}^z}{|\vec{\mathcal{S}}|}\right),$$

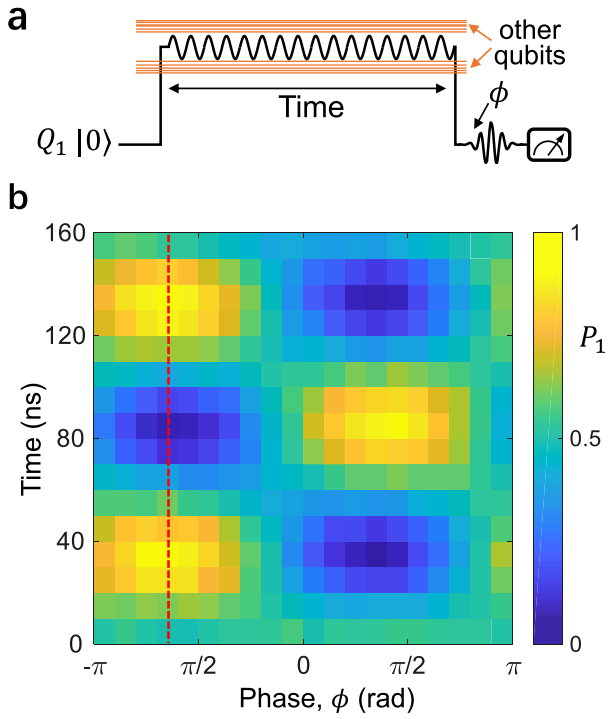

FIG. 8. **Phase alignment of the rotation pulse. a**, Experimental sequence taking Q_1 as an example. The qubit Q_1 is detuned from the resonator bus $\mathcal{R}$ by about $\Delta/2\pi \simeq -450$ MHz, while other qubits are arranged in the vicinity of this point to minimise Z-crosstalk effects. Simultaneously, we apply on Q_1 resonant microwave drives with a magnitude of $h^x/2\pi \simeq 5$ MHz, after which we quickly bias Q_1 to its idle point and apply a rotation pulse with a specific phase ϕ before the readout. **b**, 2D graph of the measured excited probabilities P_1 as a function of t and ϕ. The phase offset pointed by the red dotted vertical line should be added to Q_1's rotation pulse to align the phases.

and

$$\phi = \begin{cases} \arccos\left(\frac{\langle \mathcal{S}^x\rangle}{|\vec{\mathcal{S}}|}\right) & \text{if} \quad \langle \mathcal{S}^y\rangle > 0 \\ 2\pi - \arccos\left(\frac{\langle \mathcal{S}^x\rangle}{|\vec{\mathcal{S}}|}\right) & \text{if} \quad \langle \mathcal{S}^y\rangle < 0 \end{cases},$$

with $|\vec{\mathcal{S}}|^2 = \langle \mathcal{S}^x\rangle^2 + \langle \mathcal{S}^y\rangle^2 + \langle \mathcal{S}^z\rangle^2$. The second step is to obtain the expression of $\mathcal{S}_{\vec{n}_\perp}$ and to minimize its variance. We can obtain two orthogonal bases, $\vec{n}_1 = (-\sin\phi, \cos\phi, 0)$ and $\vec{n}_2 = (\cos\theta\cos\phi, \cos\theta\sin\phi, -\sin\theta)$, perpendicular to $\vec{n}_0$. Then, $\mathcal{S}_{\vec{n}_\perp}$ can be represented as $\vec{\mathcal{S}}\cdot\vec{n}_\perp$, with $\vec{n}_\perp = \vec{n}_1\cos\vartheta + \vec{n}_2\sin\vartheta$ and $\vartheta \in [0, 2\pi]$. The minimum in Eq. (2) of the main text is actually equivalent to the optimisation of ϑ. It turns out that the optimum procedure finally gives an elegant formula

$$\xi^2 = \frac{2}{N}[\langle(\mathcal{S}^{\vec{n}_1})^2 + (\mathcal{S}^{\vec{n}_2})^2\rangle + \sqrt{\langle(\mathcal{S}^{\vec{n}_1})^2 - (\mathcal{S}^{\vec{n}_2})^2\rangle^2 + \langle\{\mathcal{S}^{\vec{n}_1}, \mathcal{S}^{\vec{n}_2}\}\rangle^2}], \quad (3)$$

with $\{\mathcal{S}^{\vec{n}_1}, \mathcal{S}^{\vec{n}_2}\} = \mathcal{S}^{\vec{n}_1}\mathcal{S}^{\vec{n}_2} + \mathcal{S}^{\vec{n}_2}\mathcal{S}^{\vec{n}_1}$.

We measure $\langle(S^{\vec{n}_1})^2\rangle$ and $\langle(S^{\vec{n}_2})^2\rangle$ by applying single-qubit rotations to move the $\vec{n}_1$ ($\vec{n}_2$) axis in the Bloch sphere to the z-axis before readout. For $\langle\{\mathcal{S}^{\vec{n}_1}, \mathcal{S}^{\vec{n}_2}\}\rangle$, it boils down to the measurement of two-spin correlators

$$\langle\{\mathcal{S}^{\vec{n}_1}, \mathcal{S}^{\vec{n}_2}\}\rangle = \frac{1}{4}(\sum_{i\neq j}\langle\sigma_i^{\vec{n}_1}\sigma_j^{\vec{n}_2}\rangle + \sum_{i\neq j}\langle\sigma_i^{\vec{n}_2}\sigma_j^{\vec{n}_1}\rangle).$$

To characterise the two spin correlators for all combinations ($16 \times 15 \times 2$), we adopt the following methods: First, we divide the 16 qubits into 2 groups randomly, e.g., $G_1^1 = \{Q_1$–$Q_8\}$ and $G_2^1 = \{Q_9$–$Q_{16}\}$. Next, we apply rotation pulses on the qubits in G_1^1 to bring the $\vec{n}_1$-axis to the z-axis, and simultaneously apply other rotation pulses on qubits in G_2^1 to bring the $\vec{n}_2$-axis to the z-axis, after which the 16-qubit joint readout is executed, yielding the probabilities $P = \{P_{00\ldots0}, P_{00\ldots1}, ..., P_{11\ldots1}\}$. Finally, by calculating $\sum_{j=1}^{2^{16}} P_j \mathcal{S}_{j,j}^{zz(G_1^1,G_2^1)}$, with $\mathcal{S}^{zz(G_1^1,G_2^1)}$ written as

$$\mathcal{S}^{zz(G_1^1,G_2^1)} = \sum_{i\in G_1^1}\sigma_i^z \sum_{j\in G_2^1}\sigma_j^z,$$

we obtain the summation of two-spin correlators for $8 \times 8 = 64$ combinations (Q_1–Q_9, Q_1–Q_{10}, ..., Q_1–Q_{16}, Q_2–Q_9, ..., Q_8–Q_{16}), i.e.,

$$P_{n_1n_2}^1(G_1^1, G_2^1) = \sum_{i\in G_1^1, j\in G_2^1}\langle\sigma_i^{\vec{n}_1}\sigma_j^{\vec{n}_2}\rangle.$$

Moreover, by exchanging the rotation pulses applied to qubits in these two groups, we can obtain

$$P_{n_2n_1}^1(G_1^1, G_2^1) = \sum_{i\in G_1^1, j\in G_2^1}\langle\sigma_i^{\vec{n}_2}\sigma_j^{\vec{n}_1}\rangle.$$

After repeating this process 5 times, where 16 qubits are divided into two different groups of equal size, we can approach $\langle\{\mathcal{S}^{\vec{n}_1}, \mathcal{S}^{\vec{n}_2}\}\rangle$ by averaging the overall results

$$\frac{16\times15}{64\times5}\sum_{i=1}^{5}[P_{n_1n_2}^i(G_1^i, G_2^i) + P_{n_2n_1}^i(G_1^i, G_2^i)].$$

This method has been verified by numerical simulations that possess a very high precision, as illustrated in Fig. 9.

Finite-size effect of the Loschmidt echo in the LMG model. The results in the main text are in good agreement with the theoretical predictions based on the LMG

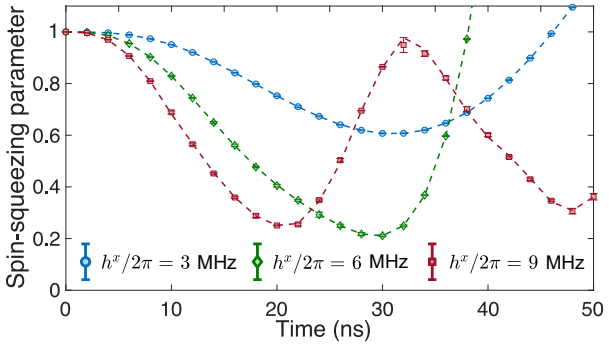

FIG. 9. **Numerical calculation of the spin-squeezing parameter.** The dashed curves are the strict results according to Eq. (3), while the points are calculated with the method described above. To estimate the error bar, we repeat the calculation 5 times for different values of t and h^x. For each time, we randomly select 5 groups of $\{G_1^i, G_2^i\}$ and average the results.

model. It has been shown that the Loschmidt echo cannot be strictly equal to 0 in a finite-size LMG model[28]. In Fig. 10a, we present the first minimum value of the Loschmidt echo $\mathcal{L}^{(1)}_{\text{min}}$ as a function of the LMG model's size N with $J = 1$ and different g, showing a perimeter law $\mathcal{L}^{(1)}_{\text{min}} \sim \exp(-\alpha N)$, with $\alpha > 0$. Although $\mathcal{L}^{(1)}_{\text{min}} \to 0$ as $N \to \infty$ for arbitrary $g > 0$, we can still observe a drastic difference of $\mathcal{L}^{(1)}_{\text{min}}$ in the two phases (Fig. 10b). Based on the above discussions, we believe that for the 16-qubit system, the value of $\mathcal{L}^{(1)}_{\text{min}}$ smaller than $\sim 10^{-2}$ can be a characteristic of the dynamical paramagnetic phase.

Possible signature of the anomalous dynamical phase. In addition to $\mathcal{L}^{(1)}_{\text{min}}$, including short-time properties of the Loschmidt echo $\mathcal{L}(t)$, the long-time evolution of $\mathcal{L}(t)$ provides more information, such as the signature of the anomalous dynamical phase, i.e., the $\mathcal{L}(t)$ may approach zero for long times, suggesting the existence of the nonanalytical point of the rate function $r(t) = -N^{-1}\log[\mathcal{L}(t)]$ in the dynamical ferromagnetic phase. The anomalous dynamical phase only exists for models with long-range interactions, and is absent for models with short-range interactions. In Fig. 11, we present the experimental data of $\mathcal{L}^{(1)}_{\text{min}}$ compared with the global minimum value of $\mathcal{L}(t)$, i.e., $\mathcal{L}^{(\text{glob.})}_{\text{min.}}$, during its dynamics with a final time $t_f \simeq 600$ ns, showing a possible signature of the anomalous dynamical phase, which can enlighten further works for investigating the anomalous dynamical phase.

Additional experimental data. In Fig.12, we plot the experimentally measured non-equilibrium order parameter as a function of the transverse field magnitude for different values of the detuning Δ. In Fig.13, we display the evolution of the experimental quasidistribution Q-function for two transverse field magnitudes.

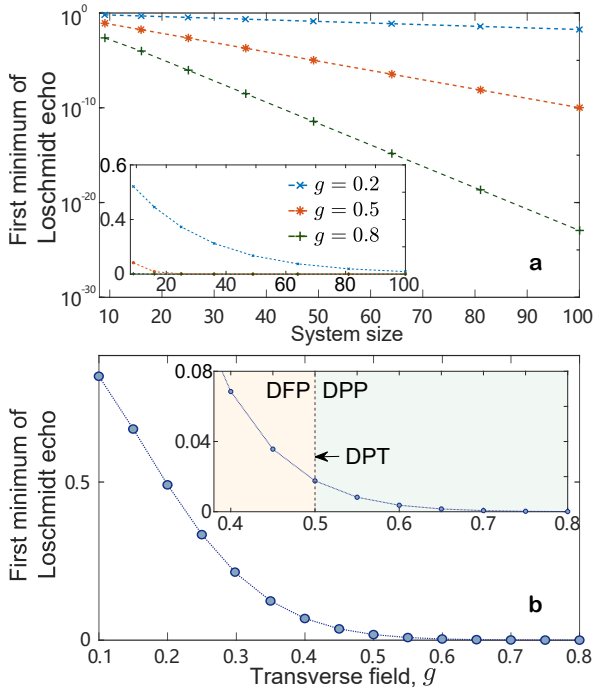

FIG. 10. **Numerical results of the Loschmidt echo in the LMG model.** **a**, The value of the first minimum of the Loschmidt echo $\mathcal{L}^{(1)}_{\text{min}}$ scales with the system's size N. **b**, The value of $\mathcal{L}^{(1)}_{\text{min}}$ as a function of g for $N = 16$.

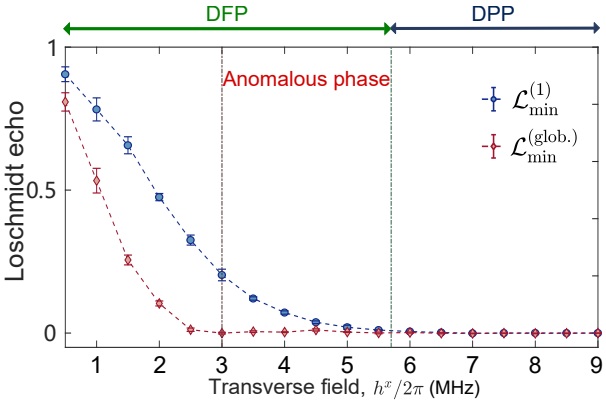

FIG. 11. **Experimental data for the long-time behaviour of the Loschmidt echo.** The value of $\mathcal{L}^{(\text{glob.})}_{\text{min}}$ as a function of h^x, with $\mathcal{L}^{(\text{glob.})}_{\text{min}}$ referring to the minimum value of the Loschmidt echo during its time evolution with a final time of around 600 ns.

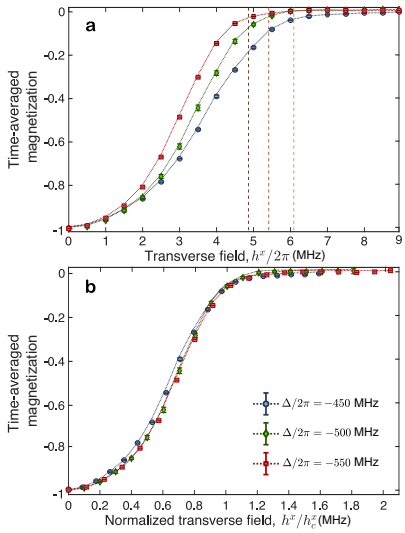

FIG. 12. **Experimental data for non-equilibrium order parameter with different values of the detuning Δ. a**, The order parameter $\overline{\langle\sigma^z\rangle}$ as a function of the field strength h^x. The theoretically predicted critical points for $\Delta/2\pi \simeq -450$ MHz, -500 MHz and -550 MHz are $h_c^x/2\pi \sim 5.7$ MHz, 5.0 MHz, and 4.4 MHz, respectively, as highlighted by the dashed vertical lines. **b**, The same data in **a** but with h^x normalized by its critical value h_c^x.

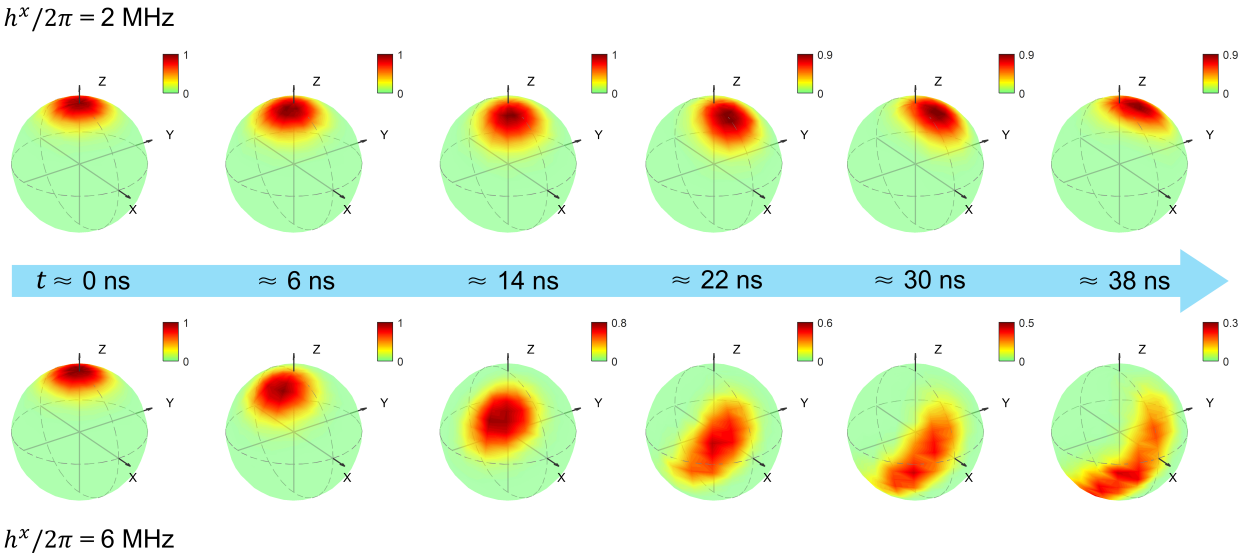

FIG. 13. **Dynamics of the quasidistribution Q-function.** The quasidistributions $Q_{\exp}(\theta, \phi)$ at different time intervals, for $h^x/2\pi$ =2 MHz (up) and 6 MHz (down), respectively.